HIGH RESOLUTION STUDY OF XENON AUTOIONIZATION USING DIRECT VUV LASER EXCITATION

A. Kortyna

Department of Physics and Astronomy, Colby College

Waterville, ME 04901

M. R. Darrach, P.-T. Howe, and A. Chutjian

Jet Propulsion Laboratory, California Institute of Technology

Pasadena, CA 91109

ABSTRACT

A new, direct vacuum ultaviolet laser excitation method is used to study the single-photon autoionization of xenon atoms in the $5p^6 \rightarrow 5p^5\ \ ns'[\frac{1}{2}]_1^0$ $(14 \leq n \leq 52)$ and $5p^6 \rightarrow 5p^5\ \ nd'[\frac{3}{2}]_1^0$ $(16 \leq n \leq 88)$ autoionizing Rydberg series. From analysis of the nd' series an ionization potential T_d = 108370.88 ± 0.05 cm^{-1} is obtained. This agrees well with a previously-reported limit of 108370.8 ± 0.2 cm^{-1}. Fano profile parameters for both series are reported, and effects of overlapping resonances is clearly seen in the series widths peaking at an effective quantum number $n^* \approx$ 50-60.

1. INTRODUCTION

The spectrum of autoionizing states of xenon in the vacuum ultraviolet (VUV) was first observed by Beutler[1] using a helium discharge lamp as the light source and a two-meter grating monochromator. Since that time the autoionization of Xe has been observed using methods[2-4] similar to those of Beutler. The most complete recent study has been by Yoshino and Freeman[5] who measured the positions of line maxima of the $5p^6 \rightarrow 5p^5\ ns'[\frac{1}{2}]_1^0$ series for $6 \leq n \leq 39$, and the $5p^6 \rightarrow 5p^5\ nd'[\frac{3}{2}]_1^0$ series for $5 \leq n \leq 65$.

The asymmetrical lineshape typical of autoionizing resonances was first analyzed using configuration interaction (CI) theory by Fano[6], with Mies[7] extending the theory to the case of overlapping channels. The photoionization cross section for the autoionizing state with quantum numbers $n\ell$ can be written in the form[8],

$$\sigma_{n\ell}(E) = \sigma_{n\ell}\frac{(q_{n\ell} + \epsilon_{n\ell})^2}{1 + \epsilon_{n\ell}^2} + \sigma_b\ , \tag{5}$$

where $\epsilon_{n\ell}$ is the energy separation from the $n\ell$ resonance in units of the half-width of the line $\frac{1}{2}\ \Gamma_{n\ell}$. For a photon energy E and a resonance energy $E_{n\ell}$, the lineshape parameter $\epsilon_{n\ell}$ is given by

$$\epsilon_{n\ell} = \frac{(E - E_{n\ell})}{\frac{1}{2}\Gamma_{n\ell}}\ , \tag{6}$$

where $\hbar/\Gamma_{n\ell}$ is the mean lifetime of the state with respect to autoionization. The quantity $\sigma_{n\ell}$ is the photoionization cross section for the autoionizing channel of quantum numbers $n\ell$, and σ_b is the direct photoionization cross section of the non-interacting continuum (or continua). The asymmetry parameter $q_{n\ell}$ in Eq. (1) is a measure of the coupling strength between the ground Xe $5p^6$ state and the $n\ell$ level modified by the continuum.

Multichannel quantum-defect theory (MQDT) provides an alternative approach to characterizing autoionization line shapes[9-15]. Specifically, MQDT can be used to generate expressions similar to that in Eq. (1)[16-18], and the parametrization in MQDT can be shown to be equivalent to that of the CI formalism[19].

The Fano parameters in Eq. (1), or those in the equivalent MQDT representation, have been determined for a number of atomic systems. Madden and Codling[20] used Eq.(1) to arrive at q and Γ values from the absorption spectrum of He. Chutjian and Carlson[21] obtained values of q in Ar through fitting the autoionization curves-of-growth. In Xe, Comes *et al.*[22] measured Γ_{nd} for $6 \leq n \leq 15$ in absorption. Bonin *et al.*[23] observed Xe^+ production using laser four-wave mixing to generate coherent vacuum ultraviolet (VUV) radiation, and measured q_{11s} and Γ_{11s}. Wu *et al.*[24] used photoelectron spectroscopy to arrive at the Fano parameters for the $8s'[\frac{1}{2}]_1^0$ and the $6d'[\frac{3}{2}]_1^0$ resonances, as well as Γ_{ns} for n = 8, 9, 10, 12, and 14. Using the MQDT formalism, Maeda *et al.*[25] fitted lineshape parameters to absorption spectra for the $ns'[\frac{1}{2}]_1^0$ $(8 \leq n \leq 14)$ and $nd'[\frac{3}{2}]_1^0$ $(10 \leq n \leq 16)$ series; and Koeckhoven *et al.*[26] fitted lineshape parameters to yield ion spectra for $ns'[\frac{1}{2}]_1^0$ $(8 \leq n \leq 14)$, $nd'[\frac{3}{2}]_1^0$ $(10 \leq n \leq 15)$, and $nd'[\frac{5}{2}]_3^0$ $(8 \leq n \leq 20)$ series, and the $5g'[\frac{7}{2}]_0^3$ state.

In the present work we have measured autoionization profiles for a wide range of principal quantum number n in both the $ns'[\frac{1}{2}]_1^0$ series ($14 \leq n \leq 52$) and the $nd'[\frac{3}{2}]_1^0$ series ($16 \leq n \leq 88$). The initial ultraviolet (UV) wavelength of 276 nm was generated by a combination of frequency doubling and mixing using a 10 Hz pulsed Nd:YAG laser. The 276 nm radiation undergoes third-harmonic generation in a pulsed jet to produce VUV radiation. The data analysis extends the works of Refs. 22-26 to significantly higher n levels in the $ns'[\frac{1}{2}]_1^0$ and $nd'[\frac{3}{2}]_1^0$ series by fitting Eq.(1) to autoionization profiles, and thus determining the lineshape parameters $q_{n\ell}$, $\Gamma_{n\ell}$ and resonance energy $E_{n\ell}$. We also note a discrepancy in the measured wavelengths for the $ns'[\frac{1}{2}]_1^0$ series as compared with those of Ref. 5, and find anomalous behavior in the values of Γ_{nd}, q_{ns}, and q_{nd} starting at about $n^* \approx 45$.

2. EXPERIMENTAL ARRANGEMENT

The photoionization apparatus consists of four major components. With reference to Fig. 1 these are: **(1)** an adjustable Nd:YAG laser system and associated nonlinear frequency-mixing components to produce intense, monochromatic, coherent UV radiation adjustable near 276.6 nm; **(2)** one chamber having a pulsed free jet of xenon serving as the nonlinear medium to produce VUV radiation near 92.2 nm *via* third-harmonic generation; **(3)** a photoionization region which is differentially-pumped with respect to the tripling chamber; photoionization takes place within a magnetically-shielded six-sided collision box electrostatically biased to reduce stray magnetic and electric fields; and **(4)** a quadrupole mass spectrometer (QMS) and associated ion focusing optics for extraction, mass analysis, and detection of the Xe^+ ions. Details of each of the components are given in the following four sections.

2.1. The Laser System

Coherent UV laser radiation is produced by nonlinear frequency conversion of a pulsed laser beam. A *Continuum, Inc.* Q-switched Nd:YAG laser produces nanosecond-wide pulses of radiation at about 1064.1 nm which are etalon-narrowed to a linewidth of 0.1 cm^{-1}. The pulse repetition rate is 10 Hz. This infrared radiation is frequency-doubled to 532.05 nm, and is used to pump a *Continuum* tunable dye laser at 573.5 nm (linewidth of 0.08 cm^{-1}). Residual 1064.1 nm radiation is then frequency-doubled a second time and mixed with the dye laser output. Mixing is carried out in a KDP^* crystal to produce 4-6 mJ/pulse of UV radiation at about 276 nm. The UV wavelength is tuned by adjusting the dye laser wavelength. During wavelength sweeps through the Rydberg series, the KDP^* crystal is maintained at optimal phase-matching conditions by an autotracking circuit.

2.2. Vacuum Ultraviolet Laser Generation

VUV radiation is generated in the range 92.0-92.8 nm with a linewidth of 0.0003 nm (0.35 cm^{-1} or 0.044 meV) through nonlinear, third-harmonic generation in a pulsed free jet of xenon[27-30]. A Xe jet provides an ideal nonlinear gaseous medium for the production of VUV radiation to probe autoionizing states approaching the $^2P^o_{1/2}$ ionization limit, because of its very uniform tripling efficiency over the wavelengths of interest[27].

Referring to Fig. 1 the 276 nm UV laser beam in air is focused by a 500 mm focal length quartz lens onto the Xe jet in the first chamber. The pulsed jet is produced by a commercial (*Lasertechnics, Inc.*) piezoelectric-actuated pulsed valve with a nozzle diameter of 0.25 mm. The beam source is mounted such that the xenon beam is directed into the throat of a 250 ℓ/s liquid-nitrogen baffled diffusion pump. Maximum tripling efficiency was found for gas pulse widths of 250-300 μs with a backing pressure of approximately 240 kPa. This corresponded to a beam pressure of about 28 kPa at one nozzle diameter from the nozzle. Pressure in the tripling chamber during operation is 1.3×10^{-2} Pa.

The tripling performance was tested through the single-photon ionization signal of xenon. In the photoionization chamber (see next *Sec. 2.3*) the VUV laser beam crossed an effusive Xe beam on the detection axis of a quadrupole mass spectrometer. The third-harmonic wavelength was held at approximately 0.005 nm above the $^2P^\circ_{1/2}$ ionization threshold where the ionization cross section is expected to be insensitive to small variations in the VUV wavelength. The third-harmonic generation efficiency, assumed to be proportional to the measured Xe^+ signal, was measured as a function of the pulsed jet backing pressure with the VUV beam focused one nozzle diameter from the nozzle. From Fig. 2, one sees that the harmonic generation efficiency reaches a maximum at about 250 kPa backing pressure, a minimum at 350 kPa, and a second broader maximum above 520 kPa. This is in qualitative agreement with earlier results[29], and is characteristic of non-phase-matched media.

The dependency of third-harmonic generation efficiency on the nozzle-laser focus distance is shown in Fig. 3. For these measurements the backing pressure was held at 280 kPa, and the nozzle was moved *via* a translation stage and micrometer. The present results are in good agreement with those of Rettner *et al.*[30] Finally, the functional dependence of the photoionization signal on the UV (276 nm) laser power was measured, and results are shown in Fig. 4. The logarithmic plot of Xe^+ signal *vs* power gave a slope of 2.9 ± 0.2, consistent with a third-order process for the 92.2 nm VUV generation.

2.3 Photoionization Region and Ion Detection

A 15 mm dia aperture placed between the tripling (third-harmonic generation) chamber and the photoionization chamber provides for differential pumping of the two chambers. The operating pressure in the photoionization chamber with all beams running is about (8-13) $\times$ 10^{-4} Pa. The unseparated VUV and UV laser wavelengths proceed together into the photoionization region. This region in enclosed by high-permeability metal shielding to reduce the ambient magnetic field. Within the photoionization chamber is a six-sided collision box which contains the Xe beam nozzle, the entrance and exit apertures for the UV/VUV beam, and an ion exit aperture. The walls of this box are electrically insulated from one another so that independent potentials may be applied to each face in order to minimize stray electric fields within the box (see *Sec. 2.4*). Pulsed ion optics and a QMS are positioned outside the box facing the ion extraction aperture. The laser beam path is crossed by an effusive Xe gas beam at the center of the nulled collision box. The Xe^+ ions formed through the ionization process are extracted by pulsed potentials applied to the sides of the nulled box and to an ion-lens element. The QMS resolution was adjusted to detect all the abundant Xe isotopes at 128-132, 134, 136 atomic mass units. The ions are detected using a channel-type electron multiplier whose output was amplified, discriminated, shaped and routed to a multichannel scaler (MCS).

The 276 nm UV laser power is monitored simultaneously with the Xe^+ data collection. Power is measured with a volume-absorber thermopile having a response time of about 1 s. The power level is digitized and transmitted to a personal computer (PC) approximately twice per second. The laser power level is averaged and stored alongside the Xe^+ data. The ion signal is corrected after the fact for laser power variations, using the third-order dependence of signal on power (Fig. 4). Autoionization spectra are accumulated in the MCS by monitoring the Xe^+ yield and the 276 nm laser power while stepping the dye laser through the wavelength range of interest.

2.4 Elimination of Stray Magnetic and Electric Fields

A high-permeability metal shield around the photoionization chamber reduced stray magnetic fields to less than 10^{-6} T. This served to minimize electron spiraling effects in electron attachment experiments (see below), and reduced Zeeman splitting effects. In terms of the Bohr magneton μ_B (5.788×10^{-2} meV/T), the total electron angular momentum J (≈ 1), and the magnetic field B (10^{-6} T), this splitting is of order of magnitude $\mu_B JB \approx 6 \times 10^{-8}$ meV, which is about six orders of magnitude less than the instrumental resolution, and hence may be neglected.

In order to minimize Stark shifts and broadening of the autoionizing resonances it is essential to reduce the level of stray electric fields in the ionization region. The two main sources of these fields are penetrating voltages from, for example, exterior lens potential; and contact potentials between conductor surfaces which might be of dissimilar metals, or be of the same metal but have a different surface history. The electric fields were minimized using a six-sided arrangement similar to that of Frey *et al.*[31]. Three pairs of parallel plates (made of chemically-pure titanium) were positioned to form a 3 cm × 3 cm × 2.5 cm box. Potentials were applied along each of three orthogonal axes with millivolt resolution to produce independently-adjustable electric fields strengths. Each applied voltage was actively filtered to reduce ripple to less than 1 mV.

Reducing the residual electric field is essential when probing high Rydberg states since small Stark shifts, unnoticed at low principal quantum numbers, can quickly obscure the closely-spaced high-n states. The minimum electric field $\mathscr{E}$ required to produce Stark-induced ℓ-mixing between adjacent n-states is given by the Inglis-Teller limit[32],

$$\mathscr{E}(mV/cm) = \frac{1.71\times10^{12}}{n^5} . \qquad (3)$$

This limit provides an estimate of the tolerable residual field strength when observing high-lying Rydberg states. The highest n observed herein was $n = 88$, so that the stray fields would have to be significantly less than $\mathscr{E}=3.23 \times 10^2$ mV/cm in order to guarantee an unperturbed state.

In practice, the ℓ-mixing itself was used as the diagnostic of electric field. The stray fields were reduced by scanning the VUV wavelength through a high-n state and adjusting the box potentials so as to minimize the linewidth of the resonance (*i.e.*, reduce the ℓ splitting). In this way we found that the fields could be monitored and reduced to within ±5 mV/cm of zero — well below the Inglis-Teller value. Once the ℓ-broadening was minimized residual field strengths could be further reduced by observing the attachment of photoelectrons to SF_6. The attachment cross section to this molecule is extremely sharply-peaked at low electron energies. By virtue of the fact that the cross section varies as (electron energy)$^{-1/2}$ one obtains attachment signals which are limited by the width of the energy distribution of the attaching photoelectrons[33]. To use this method, a small amount (approximately 10%) of SF_6 was admixed to the Xe target beam, and the laser scanned across the $^2P^o_{1/2}$ ionization threshold, thus producing photoelectrons of energy given by the difference between the photon energy and the threshold energy. These electrons are then free to attach to the admixed SF_6 to form SF_6^-. The energy dependence of the electron attachment is established by scanning the dye laser wavelength while monitoring the SF_6^- signal with the QMS. This technique is analogous to that of Ref. 33, except that the ionization here is carried out with a laser rather than with VUV from a gas discharge. Bias fields were adjusted to minimize the width of this zero-energy SF_6 resonance. Careful analysis of the attachment peak showed that the electric fields were reduced reproducibly to below 1 mV/cm[34].

3. RESULTS AND ANALYSIS

The single-photon autoionization spectrum of Xe was measured between the $^2P^o_{3/2}$ and $^2P^o_{1/2}$ ionization limits. The spectra are shown in Fig. 5 for the interval $\lambda > 92.78$ nm, and in Fig. 6 for $\lambda < 92.37$ nm. The spectra show the narrow $ns'[\frac{1}{2}]_1^0$ series, and the adjacent broader $nd'[\frac{3}{2}]_1^0$ series. The wavelength scale was calibrated by comparing the energies E_{nd} with those published by Yoshino and Freeman[5]. In the course of this calibration it was found that there was a small but significant difference with the presently-measured energies E_{ns} for the *ns'* series. These differences $\delta\lambda$ are illustrated in Fig. 7, and they average $(6 \pm 2) \times 10^{-4}$ nm, or about twice the laser linewidth. We attribute this discrepancy to the fact that the wavelength at *peak intensity* was used in Ref. 5, whereas the wavelengths in the present work were arrived at by *fitting line shapes* in the adjacent *ns'* and *(n-2)d'* levels. The agreement for the *nd'* levels was $(0.1 \pm 0.2) \times 10^{-4}$ nm, or within experimental uncertainty.

3.1 Lineshape Parameters

A fitting procedure using a double Fano profile was used to locate peak level energies in the present study. The energies E_{ns} and E_{nd} were two of the fitting parameters. The nonconstant background beneath each $ns'[\frac{1}{2}]_1^0$ peak, attributable to the adjacent $(n-2)d'[\frac{3}{2}]_1^0$ peak, leads to a slight shift of the peak of ion production away from the true resonance energy; however, the fitting procedure used herein to determine E_{ns} is insensitive to even rapidly changing backgrounds caused by the intensity and position of the adjacent $(n-2)d'[\frac{3}{2}]_1^0$ resonance.

Assuming an absence of *s'-d'* coupling (non-interacting resonances) we parametrized the autoionization lineshape by fitting the sum of two adjacent Fano profiles[24] to the experimentally-measured profiles. In terms of the Fano parameters

q_{nl} and ϵ_{nl} for the individual series, one has

$$\sigma_n(E) = \sigma_{ns}\frac{(q_{ns} + \epsilon_{ns})^2}{1 + \epsilon_{ns}^2} + \sigma_{(n-2)d}\frac{(q_{(n-2)d} + \epsilon_{(n-2)d'})^2}{1 + \epsilon_{(n-2)d}^2} + \sigma_b , \tag{4}$$

where ϵ_{nl} is defined as in Eq. (2). The parameters were determined through a least-squares fitting procedure aided by the Levenberg-Marquardt method of searching parameter space[35]. It is expected that the noncoupling assumption will break down when the spacings between the adjacent *ns'* and *(n-2)d'* members approach their combined linewidths[7], a condition present in our data starting at $n^* \approx 45$. Since absolute photoionization cross sections were not measured, values of the cross sections σ_{ns} , σ_{nd} , and σ_b were not determined.

The line profile parameters E_{ns} , Γ_{ns} and q_{ns} obtained from the fits *via* Eq. (4) for the $ns'[\frac{1}{2}]_1^0$ series are listed in Table 1 at values of the principal quantum number $14 \le n \le 52$. Present and previous values of Γ_{ns} and q_{ns} are shown in Figs. 8 and 9, respectively. One sees in Fig. 8 excellent agreement of the present widths Γ_{ns} with earlier data [23-25]. The present data extend previous measurements from $n^*=10$ to $n^*=18$, and give excellent agreement with the expected $1/n^{*3}$ dependence. Measurements at $n^* > 18$ were not possible due to lack of sufficient resolution.

The parameters E_{nd}, Γ_{nd}, and q_{nd} for the $nd'[\frac{3}{2}]_1^0$ series are listed in Table 2 for the range $16 \le n \le 88$. Values of Γ_{nd} and q_{nd} are represented in Figs. 10 and 11, respectively, with comparison to earlier data. Present values are consistent with those reported by other workers[2,22,24,25,36]. At higher n, Γ_{nd} begins to approach the instrumental linewidth (the laser linewidth of ~0.04 meV). It then becomes necessary to deconvolute the experimental lineshape using a function that is representative of the instrumental lineshape to obtain the natural linewidth. In the present study the instrumental lineshape is well-described by a Lorentzian form, allowing us to use the deconvolution technique of Wu, *et al.* [24] The Γ_{nd} values in Table 2 and Fig. 8 are results of this deconvolution.

Present measurements have extended the Γ_{nd} to significantly higher n than previously reported; and exhibit the expected $1/n^{*3}$ dependence for $n^* \leq 45$. Above an effective quantum number $n^* \approx 45$, however, Γ_{nd} deviates from the $1/n^{*3}$, showing a local maximum for n^* at about 50 (see below).

Although the resonance widths decrease approximately as n^{*3}, the separation between adjacent *ns'* and *(n-2)d'* lines decreases faster than n^{*3}. The resonance widths then become comparable to the energy separation, leading to the possibility of coupling between the two autoionization channels. It is expected that the coupled profile will differ from the simple incoherent superposition of the individual Fano profiles[8]. Hence the simple sum in Eq. (4) may not be appropriate for defining the new Γ, q. The local maximum near $n^* = 50$ (Fig. 10) may be the result of such a perturbation.

Figure 9 shows the behavior of the asymmetry parameters q_{ns} series, and Fig. 11 that for the q_{nd} series. These parameters have been shown to be relatively insensitive to instrumental linewidth[25]. For the *ns'* series there is good overlap of present and previous measurements. Overlapping measurements were not made for the *nd'* series, and present values of q_{nd} appear to be slightly higher than previously observed[24,25], although the deviation is probably within experimental error. Asymmetry parameters for both series are fairly constant as a function of n, but show a significant maximum at $n \approx 48$ and 58 for q_{ns} and q_{nd}, respectively. This may be related to the strong coupling between the ns' and $(n\text{-}2)d'$ series, and the inadequacy of Eq. (4) to describe this coupling. Such a breakdown was predicted by Mies[7] who found non-vanishing cross terms when the interval between series members became small.

3.2 Ionization Potential and Effective Quantum Numbers

The ionization limit to the $^2P^\circ_{1/2}$ state can be obtained using observed values of energies of the ns' and nd' Rydberg members. The series limit T_ℓ derived from the $n\ell$ series can be calculated from the Rydberg formula,

$$T_\ell = E_{n\ell} + \frac{\mathbb{R}}{(n-\delta_\ell)^2}\ , \qquad (5)$$

where $\mathbb{R}$ is the Rydberg constant and δ_ℓ is the Rydberg correction for the $n\ell$ series. The value of T_ℓ and δ_ℓ are used as adjustable parameters in fitting Eq. (5) to the energy term values $E_{n\ell}$ using a least-squares fitting procedure. This gives a limit for the ns' series of T_s = 108371.23 ± 0.05 cm^{-1} and a Rydberg correction δ_s = 4.01. The nd' series limit is T_d = 108370.88 ± 0.05 cm^{-1} with δ_d = 2.29. The errors quoted in the two ionization limits are derived from the 1σ uncertainty in the least-squares fitting procedure.[37] It is noted that the ns' series limit does not agree within the uncertainty with the nd' limit. It is suspected that the perturbation caused by the ns' — nd' coupling skews the calculated ns' limit more strongly than the limit calculated from the experimentally more complete nd' series. Hence T_d is expected to be the more accurate value. In fact, T_d agrees with the limit of Yoshino and

Freeman (108370.8 ± 0.2 cm^{-1})[5] and Moore (108371.0 cm^{-1})[38]. The present values of δ_ℓ are also in good agreement with a value δ_s = 4.0053 of Ref. 24; and δ_s = 4.00 and δ_d = 2.32 of Ref. 36. Other experimental values are given by Koeckhoven *et al.*[26] as δ_s = 4.021 ± 0.006 and δ_d = 2.33 ± 0.03; Wang and Knight[39] as δ_s = 4.013 ± 0.002 and δ_d = 2.32 ± 0.01; and Geiger[40] as δ_s = 3.987 and δ_d = 2.299. Johnson *et al.*[41] give theoretically-calculated values of δ_s = 3.981 and δ_d = 2.286.

Upon establishing the $^2P^o_{1/2}$ ionization limit Eq. (5) was inverted to obtain an estimate of the effective principal quantum number $n_\ell^* = n - \delta_\ell$ for members of the *ns'* and *nd'* series. These effective quantum numbers are listed in the columns of Tables 1 and 2.

4. CONCLUSIONS

Single-photon, vacuum ultraviolet (92.2 nm) laser-ionization spectroscopy was used to study the xenon autoionization spectra through the $ns'[\frac{1}{2}]_1^0$ and $nd'[\frac{3}{2}]_1^0$ Rydberg series. The Fano profile parameters q_{ns}, q_{nd}, Γ_{ns} and Γ_{nd} were determined for the *ns'* series in the range 14 ≤ *n* ≤52, and for the *nd'* series in the range 16 ≤ *n* ≤ 88. The present analysis extends previous analyses to significantly higher *n*. It is found that at *n* below about 45 the present results are in good agreement with other measurements. Anomalous behavior of the Fano parameters above *n* ≈ 50-60 is very likely due to interfering resonance structures as the spacing between adjacent *ns'* and *(n-2)d'* levels approaches the combined linewidths of the levels. The $^2P^o_{1/2}$ ionization limit was found to be T_d = 108370.88 ± 0.05 cm^{-1}, in good agreement with the previous measurement of T_d = 108370.8 ± 0.2 cm^{-1}.

ACKNOWLEDGMENTS

We thank V. Garkanian for his contributions to this project. This work was carried out at the Jet Propulsion Laboratory, California Institute of Technology, and was supported by the National Science Foundation through agreement with the National Aeronautics and Space Administration.

REFERENCES

[1] H. Beutler, "Über Absorptionsserien von Argon, Krypton und Xenon in Termen Zwischen den Beiden Ionisierungsgrenzen $^2P_{3/2}$ und $^2P_{1/2}$," Z. Phys. **93**, 177-191 (1935).

[2] R. E. Huffman, Y. Tanaka, and J. C. Larrabee, "Absorption Coefficients of Xenon and Argon in the 600-1025 Å Wavelength Regions," J. Chem. Phys. **39**, 902-909 (1963).

[3] F. M. Matsunaga, R. S. Jackson, and K. Watanabe, "Photoionization Yield and Absorption Coefficient of Xenon in the Region of 860-1022 Å," J. Quant. Spectrosc. Rad. Transfer **5**, 329-333 (1965).

[4] P. H. Metzger and G. R. Cook, "Flux Distribution of the Hopfield Helium Continuum from the Photoionization of Ar, Kr, and Xe," J. Opt. Soc. Am. **55**, 516-520 (1965).

[5] K. Yoshino and D. E. Freeman, "Absorption Spectrum of Xenon in the Vacuum-Ultraviolet Region," J. Opt. Soc. Am. B **2**, 1268-1274 (1985).

[6] U. Fano, "Effects of Configuration Interaction on Intensities and Phase Shifts," Phys. Rev. **124**, 1866-1878 (1961).

[7] F. H. Mies, "Configuration Interaction Theory: Effects of Overlapping Resonances," Phys. Rev. **175**, 164-175 (1968).

[8] U. Fano and J. W. Cooper, "Line Profiles in the Far-UV Absorption Spectra of the Rare Gases," Phys. Rev. **137**, A1364-A1379 (1961).

[9] U. Fano, "Unified Treatment of Perturbed Series, Continuous Spectra, and Collisions," J. Opt. Soc. Am. **65**, 979-987 (1975).

[10] M. J. Seaton, "Quantum Defect Theory I. General Formulation," Proc. Phys. Soc. **88**, 801-814 (1966); M. J. Seaton, "Quantum Defect Theory II. Illustrative One-Channel and Two-Channel Problems," Proc. Phys. Soc. **88**, 815-832 (1966); W. Eissner, H. Nussbaumer, H. E. Saraph, and M. J. Seaton, "Resonance in Cross Sections for Excitation of Forbidden Lines in O^{2+}," J. Phys. B **2**, 341-355 (1969).

[11] C. H. Greene, A. R. P. Rau, and U. Fano, "General Form of the Quantum-Defect Theory II." Phys. Rev. A **26**, 2441-2459 (1982).

[12] D. A. Harmin, "Hydrogenic Stark Effect: Properties of the Wavefunction," Phys. Rev. A **24**, 2491-2517 (1981); D. A. Harmin, "Theory of the Stark Effect," Phys. Rev. A **26**, 2656-2681 (1982).

[13] F. H. Mies, "A Multichannel Quantum Defect Analysis of Diatomic Predissociation and Inelastic Atomic Scattering," J. Chem. Phys. **80**, 2514-2525 (1984); F. H. Mies and P. S. Julienne, "A Multichannel Quantum Defect Analysis of Two-State Couplings in Diatomic Molecules," J. Chem. Phys. **80**, 2526-2536 (1984).

[14] W. L. Cooke and C. L. Cromer, "Multichannel Quantum-Defect Theory and an Equivalent N-Level System," Phys. Rev. A **32**, 2725-2738 (1985).

[15] K. Ueda, "Spectral Line Shapes of Autoionizing Rydberg Series of Xenon," J. Opt. Soc. Am. B **4**, 424-427 (1987).

[16] J. P. Connerade, "On Rydberg Series of Autoionizing Resonances," J. Phys. B. **16**, L329-335 (1983).

[17] J. Dubau and M. J. Seaton, "Quantum Defect Theory XIII. Radiative Transitions," J. Phys. B **17**, 381-403 (1984).

[18] A. Giusti-Suzor and U. Fano, "Alternative Parameters of Channel Interactions: I. Symmetry Analysis of the Two-Channel Coupling," J. Phys. B **17**, 215-230

(1984); A. Giusti-Suzor and U. Fano, "Alternative Parameters of Channel Interactions: II. A Hamiltonian Model," J. Phys. B **17**, 4267-4275 (1984); A. Giusti-Suzor and U. Fano, "Alternative Parameters of Channel Interactions: III. Note on a Narrow Band in the Ba $J=2$ Spectrum," J. Phys. B **17**, 4277-4283 (1984).

[19] K. Ueda, "Spectral Shapes of Autoionizing Rydberg Series," Phys. Rev. A **35**, 2484-2492 (1987).

[20] R. P. Madden and K. Codling, "Two-Electron Excitation States in Helium," Astrophys. J. **141**, 364-375 (1965).

[21] A. Chutjian and R. Carlson, "Curves of Growth of Autoionizing Spectral Lines with Application to the 3s-4p Transition in Argon," J. Opt. Soc. Am. **60**, 1204-1208 (1970).

[22] F. J. Comes, H. G. Sälzer, and G. Schumpe, "Autoionisation in Atomspektren," Z. Naturforsch. **23a**, 137-151 (1967).

[23] K. D. Bonin, T. J. McIlrath and K. Yoshino, "High-Resolution Laser and Classical Spectroscopy of Xenon Autoionization," J. Opt. Soc. Am. B **2**, 1275-1283 (1985).

[24] J. Z. Wu, S. B. Whitfield, C. D. Caldwell, M. O. Krause, P. van der Meulen, and A. Fahlman, "High-Resolution Photoelectron Spectrometry of Selected *ns'* and *nd'* Autoionization Resonances in Ar, Kr, and Xe," Phys. Rev. A **41**, 1350-1357 (1990).

[25] K. Maeda, K. Ueda, T. Namioka, and K. Ito, "High-Resolution Measurement of Beutler-Fano Profiles for Autoionizing Rydberg Series of Xe," Phys. Rev. A **45**, 527-530 (1992); K. Maeda, K. Ueda, T. Namioka, and K. Ito, "High-Resolution

Measurement for Photoabsorption Cross Sections in the Autoionization Regions of Ar, Kr, and Xe," J. Phys. B **26**, 1541-1555 (1993).

[26] S. M. Koeckhoven, W. J. Buma, and C. A. de Lange, "Three-Photon Excitation of Autoionizing States of Ar, Kr, and Xe between the $^2P_{3/2}$ and $^2P_{1/2}$ Ionic Limits," Phys. Rev. A **49**, 3322-3332 (1994).

[27] R. H. Page, R. J. Larkin, A. H. Kung, Y. R. Shen, and Y. T. Lee, "Frequency Tripling into the 720-1025 Å Region with Pulsed Free Jets," Rev. Sci. Instr. **58**, 1616-1620 (1987).

[28] E. E. Marinero, C. T. Rettner, R. N. Zare, and A. H. Kung, "Excitation of H_2 Using Continuously Tunable Coherent XUV Radiation (97.3-102.3 nm)," Chem. Phys. Lett. **95**, 486-491 (1983).

[29] A. H. Kung, "Third-Harmonic Generation in a Pulsed Supersonic Jet of Xenon," Opt. Lett. **8**, 24-26 (1983).

[30] C. T. Rettner, E. E. Marinero, R. N. Zare, and A. H. Kung, "Pulsed Free Jets: a Novel Nonlinear Media for Generation of Vacuum Ultraviolet and Extreme Ultraviolet Radiation," J. Chem. Phys. **88**, 4459-4465 (1984).

[31] M. T. Frey, L. Ling, B. G. Lindsay, K. A. Smith, and F. B. Dunning, "Use of the Stark Effect to Minimize Residual Electric Fields in an Experimental Volume," Rev. Sci. Instr. **64**, 3649-3650 (1993).

[32] W. A. Chupka, "Factors Affecting Lifetimes and Resolutions of Rydberg States Observed in Zero-Electron-Kinetic-Energy Spectroscopy," J. Chem. Phys. **98**, 4520-4530 (1993); F. Merkt, H. H. Fielding, and T. P. Softley, "Electric Field Effects on Zero-Kinetic-Energy-Photoelectron Spectra: An Explanation of Observed Trends," Chem. Phys. Lett. **202**, 153-160 (1993).

[33] A. Chutjian and S. H. Alajajian, "*s*-Wave Threshold in Electron Attachment: Observations and Cross Sections in CCl_4 and SF_6 at Ultralow Electron Energies," Phys. Rev. A **31**, 2885-2892 (1985).

[34] A. Kortyna, M. Darrach, P-T. Howe, and A. Chutjian, in preparation.

[35] W. H. Press, B. P. Flannery, S. A. Teukkolsky, and W. T. Vetterling, *Numerical Recipes: The Art of Scientific Computing* (Cambridge, UK, 1983) pp. 521-528.

[36] K. Radler and J. Berkowitz, "Photoionization Mass Spectrometry of Neon Using Synchrotron Radiation: Anomalous Variations of Resonance Widths in the Noble Gases," J. Chem. Phys. **70**, 216-220 (1979).

[37] J. R. Taylor, *An Introduction to Error Analysis* (Univ. Science Books, Mill Valley, CA, 1997) pp. 181-197.

[38] C. E. Moore, *Ionization Potentials and Ionization Limits Derived From the Analyses of Optical Spectra*, NSRDS-NBS 34 (U. S. Government Printing Office, Washington DC, 1970).

[39] L. Wang and R. D. Knight, "Two-Photon Laser Spectroscopy of *ns'* and *nd'* Autoionizing Rydberg Series in Xenon," Phys. Rev. A **34**, 3902-3907 (1986).

[40] J. Geiger, "Energy Loss Spectra of Xenon and Krypton and Their Analysis by Energy-Dependent Multichannel Quantum Defect Theory," Z. Physik A **282**, 129-141 (1977).

[41] W. R. Johnson, K. T. Cheng, K-N. Huang, and M. Le Dourneuf, "Analysis of Beutler-Fano Autoionizing Resonances in the Rare-Gas Atoms Using the Relativistic Quantum-Defect Theory," Phys. Rev. A **22**, 989-997 (1980).

Table 1. Quantum Numbers, Energy Levels, and Fano q, $\Gamma_{n\ell}$ Parameters for the Xe(ns) Series

n	n^*	wavelength (nm)	E_{ns} (cm^{-1})	q_{ns}	Γ_{ns} (meV)
14	9.98	93.2263	107270.1	16	0.176
18	13.98	92.75577	107810.0	11	0.041
19	14.99	92.69323	107882.7	17	0.039
20	15.99	92.64230	107942.0	26	0.026
21	16.98	92.60046	107990.8	26	---
22	17.98	92.56544	108031.7	17	---
23	18.99	92.53535	108066.8	19	---
24	19.99	92.50977	108096.7	19	---
25	21.00	92.48781	108122.4	23	---
26	22.01	92.46872	108144.7	23	---
27	23.01	92.45223	108164.0	21	---
28	24.00	92.43795	108180.7	16	---
29	24.98	92.42539	108195.4	16	---
30	25.99	92.41392	108208.8	22	---
31	27.01	92.40369	108220.8	25	---
32	28.01	92.39471	108231.3	17	---
33	28.97	92.38686	108240.5	13	---
34	30.02	92.37920	108249.4	17	---
35	30.96	92.37301	108256.7	17	---
36	31.97	92.36694	108263.8	8??	---
37	33.00	92.36132	108270.4	26	---
38	33.99	92.35638	108276.2	22	---
39	35.02	92.35168	108281.7	25	---
40	35.99	92.34761	108286.5	20	---
41	36.97	92.34385	108290.9	17	---
42	37.98	92.34025	108295.1	19	---
43	38.95	92.33707	108298.9	36	---

44	39.98	92.33392	108302.6	43	---
45	40.95	92.33116	108305.7	140	---
46	41.95	92.32854	108308.9	46	---
47	42.96	92.32609	108311.7	110	---
48	43.95	92.32381	108314.4	98	---
49	44.94	92.32172	108316.9	97	---
50	46.01	92.31959	108319.4	96	---
51	46.88	92.31796	108321.3	84	---
52	47.93	92.31612	108323.4	110	---

Table 2. Quantum Numbers, Energy Levels, and Fano q, $\Gamma_{n\ell}$ Parameters for the Xe(nd) Series

n	*n**	*wavelength (nm)*	E_{nd} (cm^{-1})	q_{nd}	Γ_{nd} (meV)
16	13.70	92.77618	107786.3	5.2	2.24
17	14.72	92.70923	107864.1	4.1	1.23
18	15.72	92.65556	107926.6	3.4	1.12
19	16.72	92.61136	107978.1	2.9	0.871
20	17.71	92.57447	108021.1	2.8	0.828
21	18.72	92.54312	108057.7	3.4	0.792
22	19.72	92.51655	108088.8	3.4	0.576
23	20.72	92.49382	108115.3	3.5	0.401
24	21.72	92.47414	108138.3	3.4	0.421
25	22.72	92.45714	108158.2	2.8	0.391
26	23.71	92.44216	108175.8	2.5	0.353
27	24.71	92.42906	108191.1	2.8	0.311
28	25.71	92.41728	108204.9	2.7	0.235
29	26.73	92.40666	108217.3	2.9	0.213
30	27.74	92.39726	108228.3	2.7	0.219
31	28.77	92.38878	108238.3	3.2	0.194
32	29.76	92.38130	108247.0	2.8	0.184
33	30.80	92.37434	108255.2	3.8	0.110
34	31.75	92.36852	108262.0	2.1	0.170
35	32.77	92.36279	108268.7	3.8	0.133
36	33.79	92.35764	108274.7	3.6	0.119
37	34.80	92.35293	108280.3	3.7	0.106
38	35.79	92.34871	108285.2	4.3	0.0948
39	36.78	92.34482	108289.8	3.9	0.115
40	37.79	92.34120	108294.0?	5.4	0.111
41	38.80	92.33782	108298.0	4.8	0.0893
42	39.81	92.33470	108301.6	4.7	0.0885

43	40.83	92.3318	108305.0	4.5	0.0799
44	41.81	92.32911	108308.2	3.8	0.0828
45	42.82	92.32666	108311.0	5.8	0.0858
46	43.82	92.32441	108313.7	5.7	0.0755
47	44.83	92.32238	108316.0	5.7	0.0667
48	45.87	92.32014	108318.7	6	0.0798
49	46.79	92.31846	108320.6	6.3	0.0845
50	47.80	92.31666	108322.8	8.2	0.091
51	48.78	92.31502	108324.7	8	0.116
52	49.73	92.31345	108326.5	16.1	0.112
53	50.68	92.31204	108328.2	19.5	0.105
54	51.64	92.31066	108329.8	10.8	0.105
55	52.61	92.3094	108331.3	10.8	0.107
56	53.76	92.30815	108332.7	19.8	0.12
57	54.76	92.30704	108334.0	18.4	0.112
58	55.79	92.30587	108335.4	19.9	0.0995
59	56.74	92.30484	108336.6	15.2	0.0926
60	57.77	92.30378	108337.9	14.8	0.0817
61	58.78	92.30278	108339.0	15.1	0.0694
62	59.73	92.30189	108340.1	18.3	0.0686
63	60.68	92.30102	108341.1	21.2	0.0683
64	61.48	92.30023	108342.0	25.2	0.0647
65	62.39	92.29949	108342.9	9.8	0.0559
66	63.30	92.29877	108343.8	5.8	0.0496
67	64.22	92.29809	108344.6	9.5	0.0804
68	65.50	92.29748	108345.3	7.3	0.067
69	66.61	92.29687	108346.0	10.2	0.0514
70	67.57	92.29631	108346.6	8.9	0.0797
71	68.43	92.29577	108347.3	11.9	0.0814
72	69.14	92.29527	108347.9	8.3	0.0844
73	70.24	92.29476	108348.5	12.6	0.0774
74	71.18	92.29428	108349.0	9.2	0.0708

75	72.22	92.29363	108349.8	9?	0.0656
76	73.49	92.29301	108350.6	10	0.0575
77	74.20	92.29269	108350.9	9.3	0.0690
78	75.19	92.22924	108351.5	8.5	0.0878
79	76.24	92.29179	108352.0	8.6	0.0427
80	77.17	92.29140	108352.5	9.3	0.0675
81	78.25	92.29097	108342.7?	13	0.0926
82	78.93	92.29071	108353.3?	14	0.120
83	79.73	92.29041	108353.6	14	0.239
84	80.83	92.29033	108353.7	14	0.175
85	81.76	92.28969	108354.5	12	0.118
86	82.06	92.28959	108354.6	8.8	0.0801
87	83.02	92.28927	108355.0	13	0.132
88	83.85	92.28900	108355.3	10	0.0734

FIGURE CAPTIONS

Figure 1. Schematic diagram of the laser photoionization apparatus. The legend is: **Nd:YAG** - 10 Hz pulsed neodymium-YAG laser; **DX** - doubling crystal; **DyL** - dye laser; **MX** - mixing crystal; **QL** - quartz focusing lens; **TC** - tripling chamber; **T** - wavelength-tripling pulsed jet (Xe); **TMP1** - 250 ℓ/s turbomolecular pump; **B** - differential pumping baffle; **IC** - ionization vacuum chamber; **NB** - electric-field nulling box; **G** - pulsed or continuous Xe target gas; **PM** - power meter to measure 276 nm power; **EC** - ion extraction cone; **IL** - ion focusing lens system; **P** - pulsed voltage on IC and first lens element; **QMS** - quadrupole mass spectrometer; **CEM** - channel-type electron multiplier; **TMP2** - 250 ℓ/s turbomolecular pump; **PA** - signal preamplifier, **PC** - personal computer, **MC** - master clock to control data acquisition and voltage pulses to **T**, **G**, and **P**.

Figure 2. Single-photon VUV ionization of Xe as a function of the pulsed-jet backing pressure. The third-harmonic generation efficiency is assumed to be proportional to the Xe^+ signal. The wavelength here is 92.271 nm. The laser is focused one nozzle diameter (0.25 mm) away from the pulsed jet. Error bars are given at the 1σ limit.

Figure 3. Single-photon VUV photoionization of Xe as a function of normalized distance x/D between the pulsed-jet nozzle (of diameter $D=0.25$ mm) and the laser focus. The third-harmonic generation efficiency is assumed to be proportional to the Xe^+ signal. The tripling medium is Xe gas at a backing pressure of 280 kPa.

Figure 4. Single-photon VUV (92.2 nm) photoionization of Xe as a function of UV (276 nm) laser power. The slope is equal to 2.9 ± 0.2 UV photons per ion, corresponding to the power law expected for a third-order process.

Figure 5. Single-photon Xe^+ yield as a function of wavelength for the wavelength region above 92.34 nm. The nozzle diameter is 0.25 mm and the xenon backing pressure 240 kPa.

Figure 6. Same as Fig. 5, except for the wavelength region below 92.37 nm.

Figure 7. Comparison of resonance positions Between Ref. 5 and present data. The $ns'[\frac{1}{2}]_1^0$ Rydberg series (○) shows an average deviation $\delta\lambda$ of $(6 \pm 2) \times 10^{-4}$ nm; whereas the $nd'[\frac{3}{2}]_1^0$ series (■) has an average deviation $\delta\lambda$ of $(0.1 \pm 0.2) \times 10^{-4}$ nm.

Figure 8. Present and previous measurements of the linewidth parameter Γ_{ns} for the $ns'[\frac{1}{2}]_1^0$ Rydberg series. Present data are solid squares (■), and other data are from Ref. 23 (Δ), Ref. 24 (▲), Ref. 25 (○) and Ref. 36 (□). Also shown is the expected $1/n^{*3}$ dependence (solid line).

Figure 9. The asymmetry parameters q_{ns} for the $ns'[\frac{1}{2}]_1^0$ Rydberg series. Present data are solid squares (■), along with data from Ref. 23 (Δ), Ref. 24 (∇), and Ref. 25 (○).

Figure 10. Present and previous measurements of the linewidth parameter Γ_{nd} for the $nd'[\frac{3}{2}]_1^0$ Rydberg series. Present data are solid squares (■), and other data are from Ref. 22 (Δ) and Ref. 25 (○). Also shown is the expected $1/n^{*3}$ dependence (solid line).

Figure 11. The asymmetry parameter q_{nd} for the $nd'[\frac{3}{2}]_1^0$ series. Present data are solid squares (■), along with data from Ref. 24 (∇) and Ref. 25 (○).

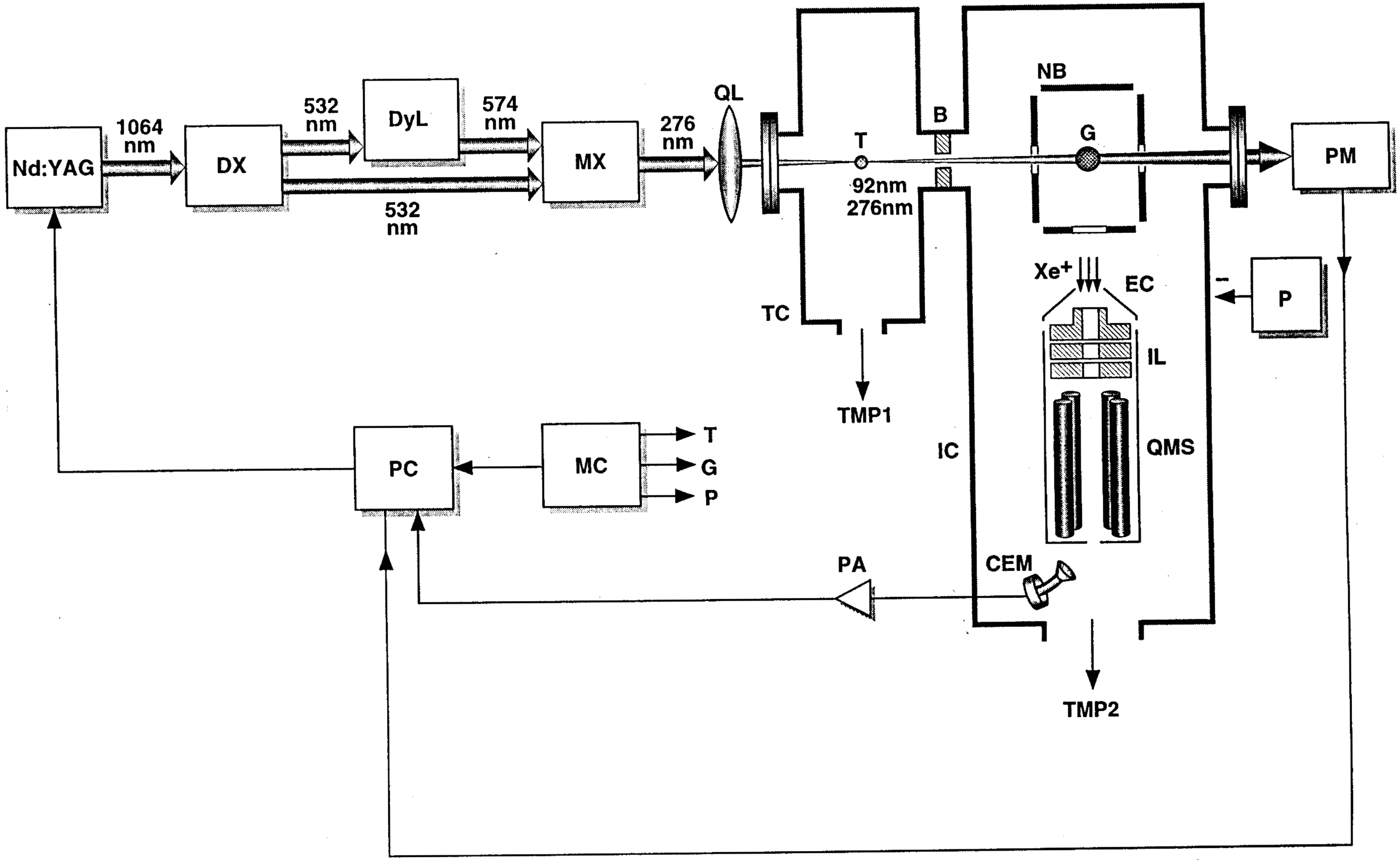
Nd:YAG
1064 nm
DX
532 nm
DyL
574 nm
532 nm
MX
276 nm
QL
T
B
NB
G
92nm
276nm
PM
TC
TMP1
Xe+
EC
IL
QMS
IC
P
PC
MC
T
G
P
PA
CEM
TMP2

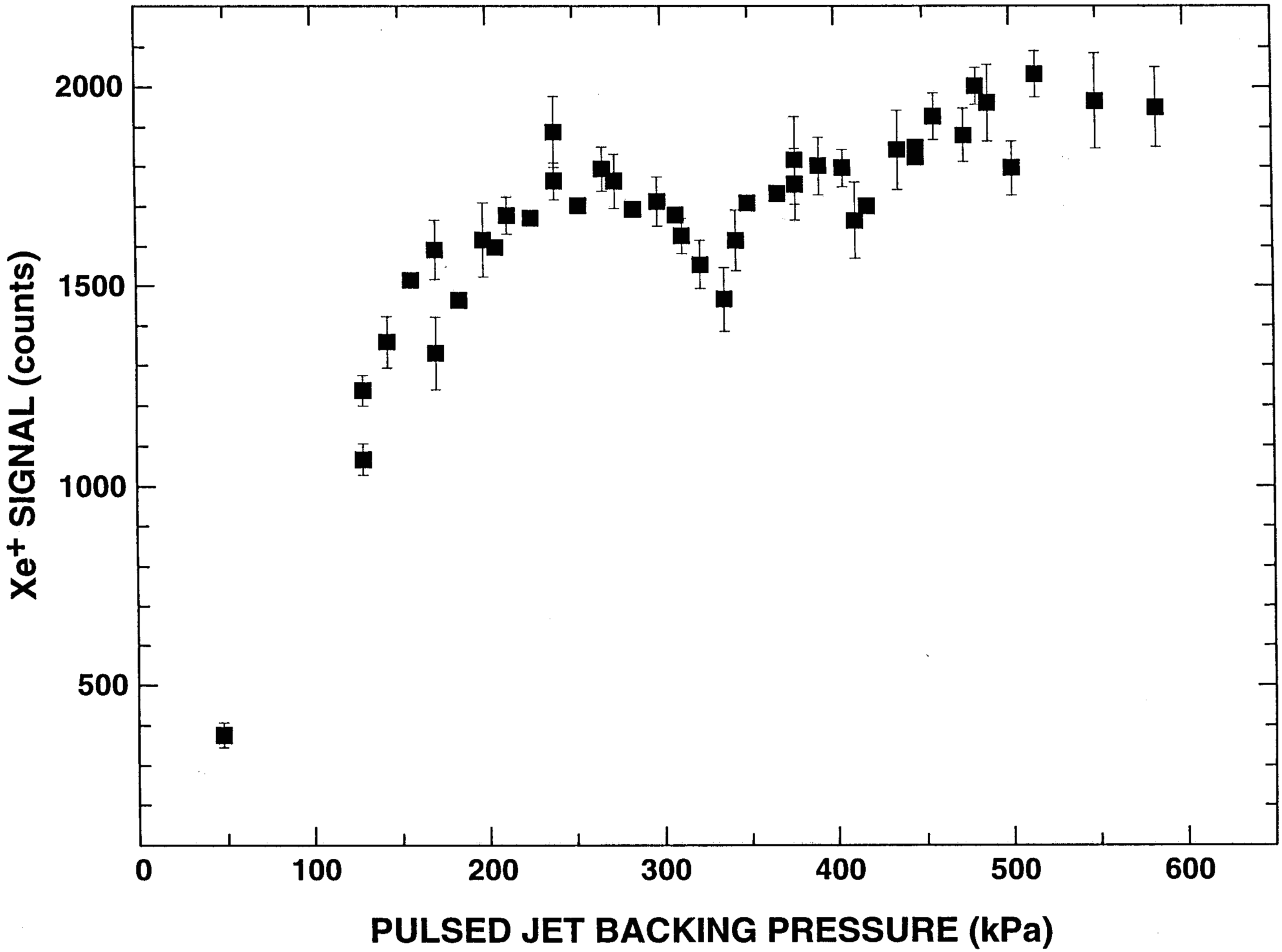

Xe+ SIGNAL (counts)
2000
1500
1000
500
0
100
200
300
400
500
600
PULSED JET BACKING PRESSURE (kPa)

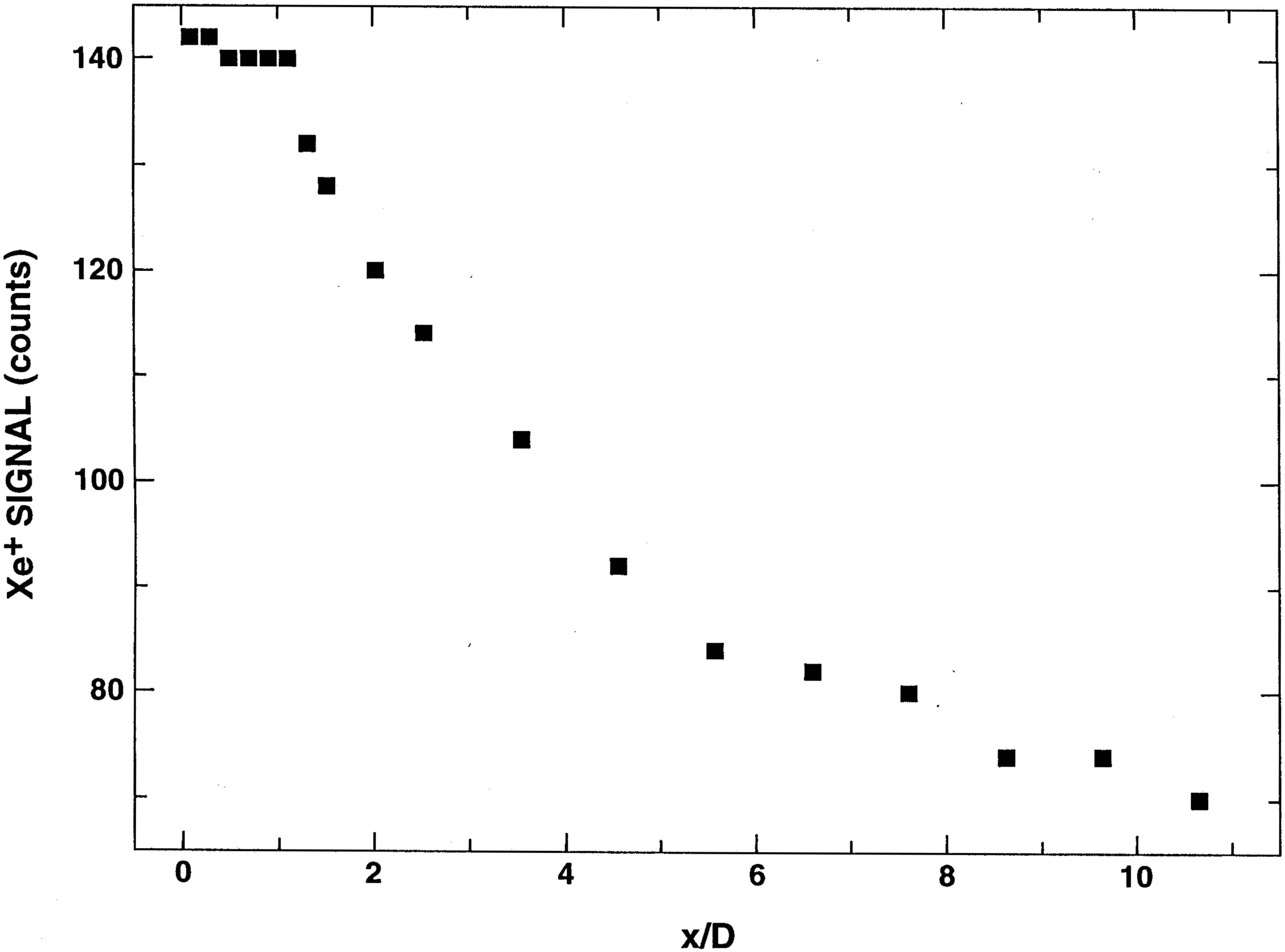

3

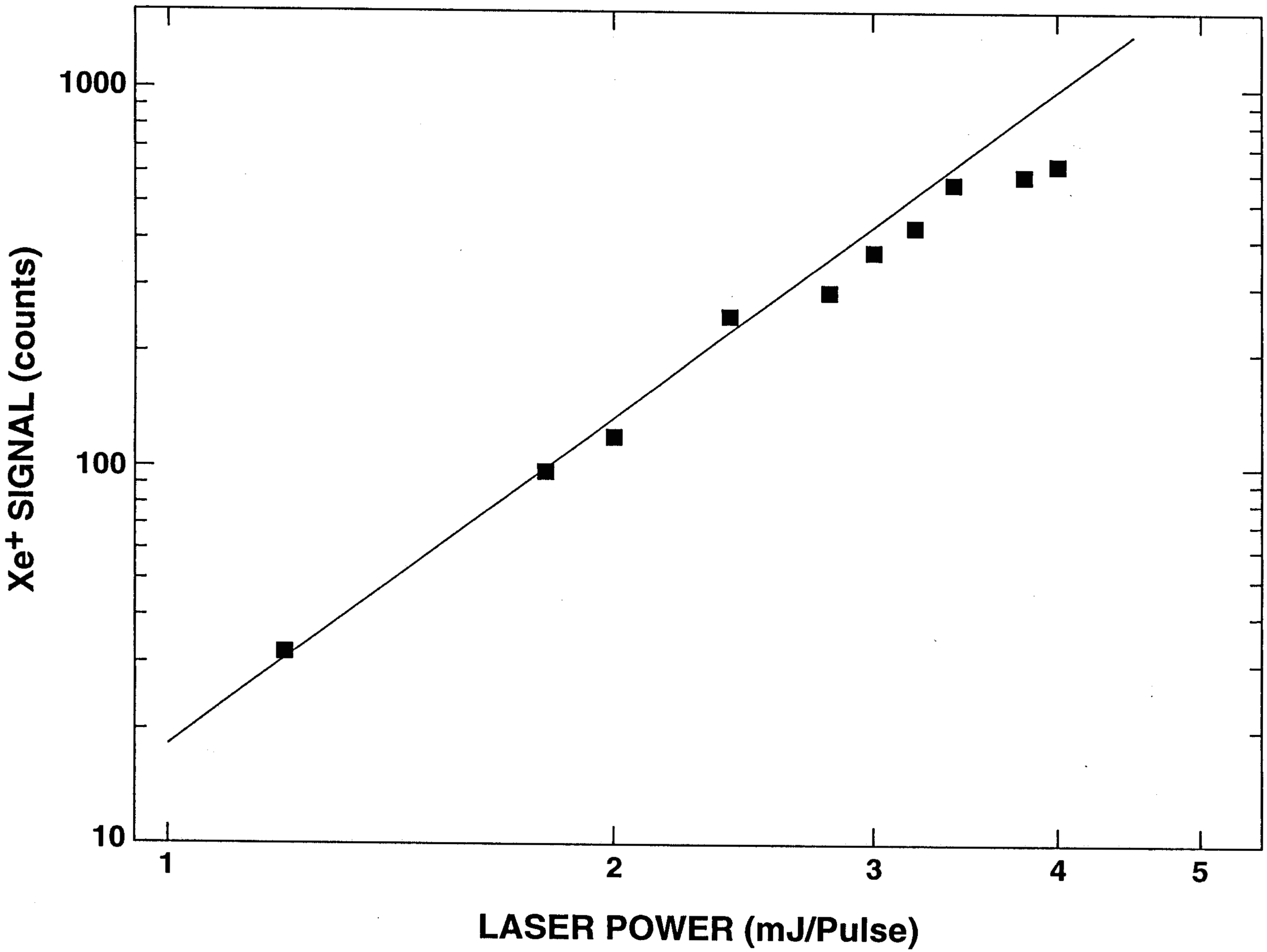

77

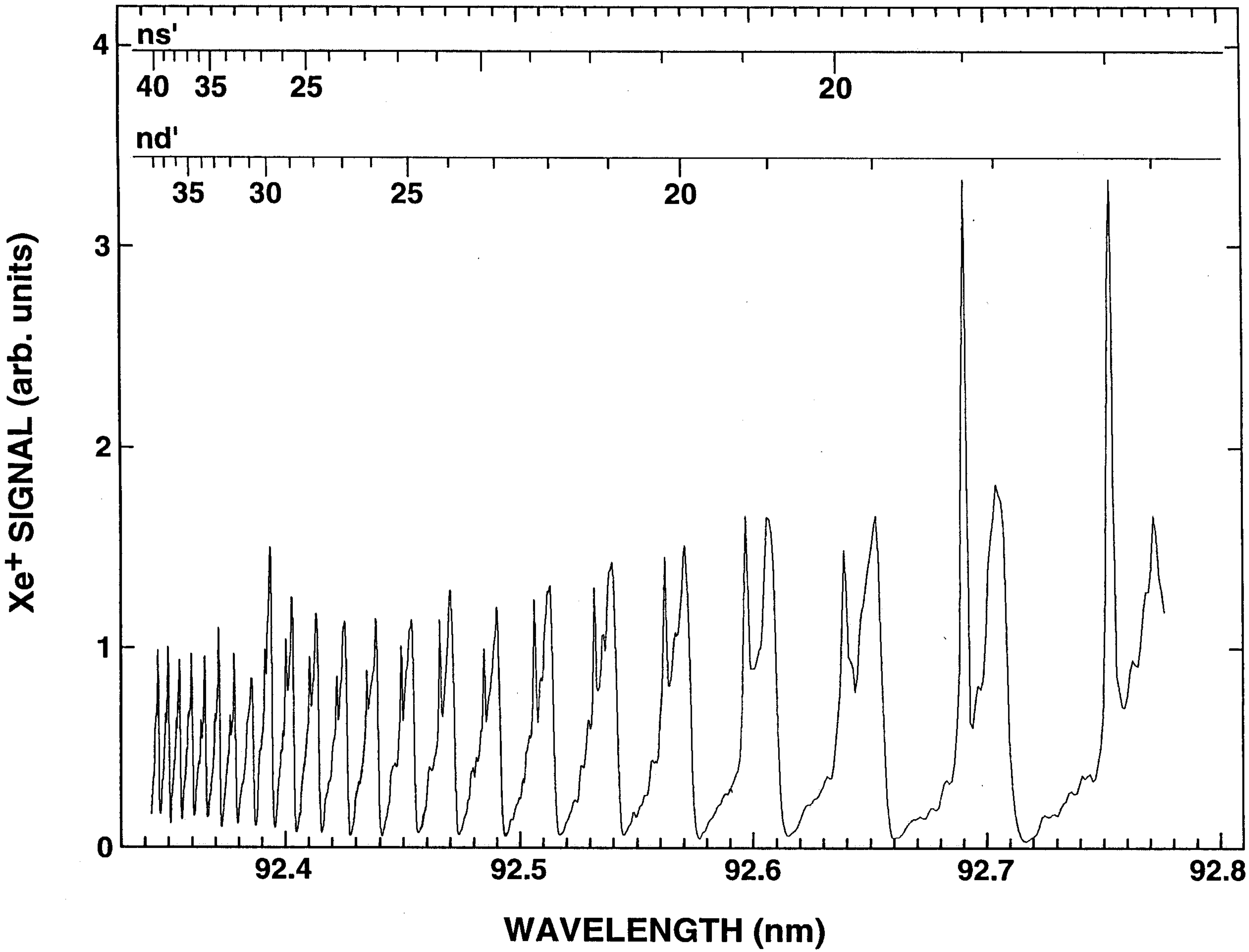

ns'
40
35
25
20
nd'
35
30
25
20
Xe$^+$ SIGNAL (arb. units)
0
1
2
3
4
92.4
92.5
92.6
92.7
92.8
WAVELENGTH (nm)

5

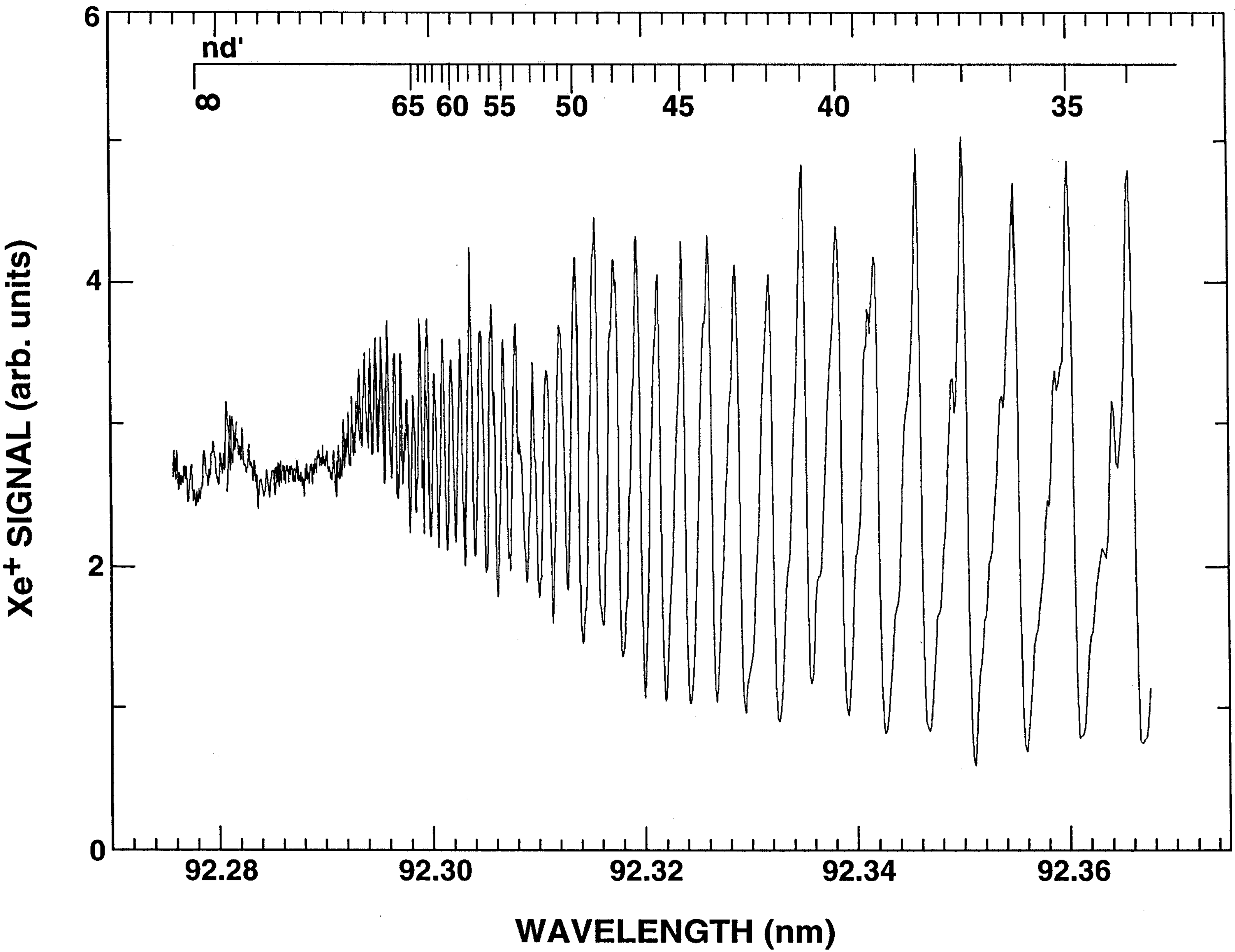
nd'
∞
65
60
55
50
45
40
35
6
4
2
0
Xe+ SIGNAL (arb. units)
92.28
92.30
92.32
92.34
92.36
WAVELENGTH (nm)

9

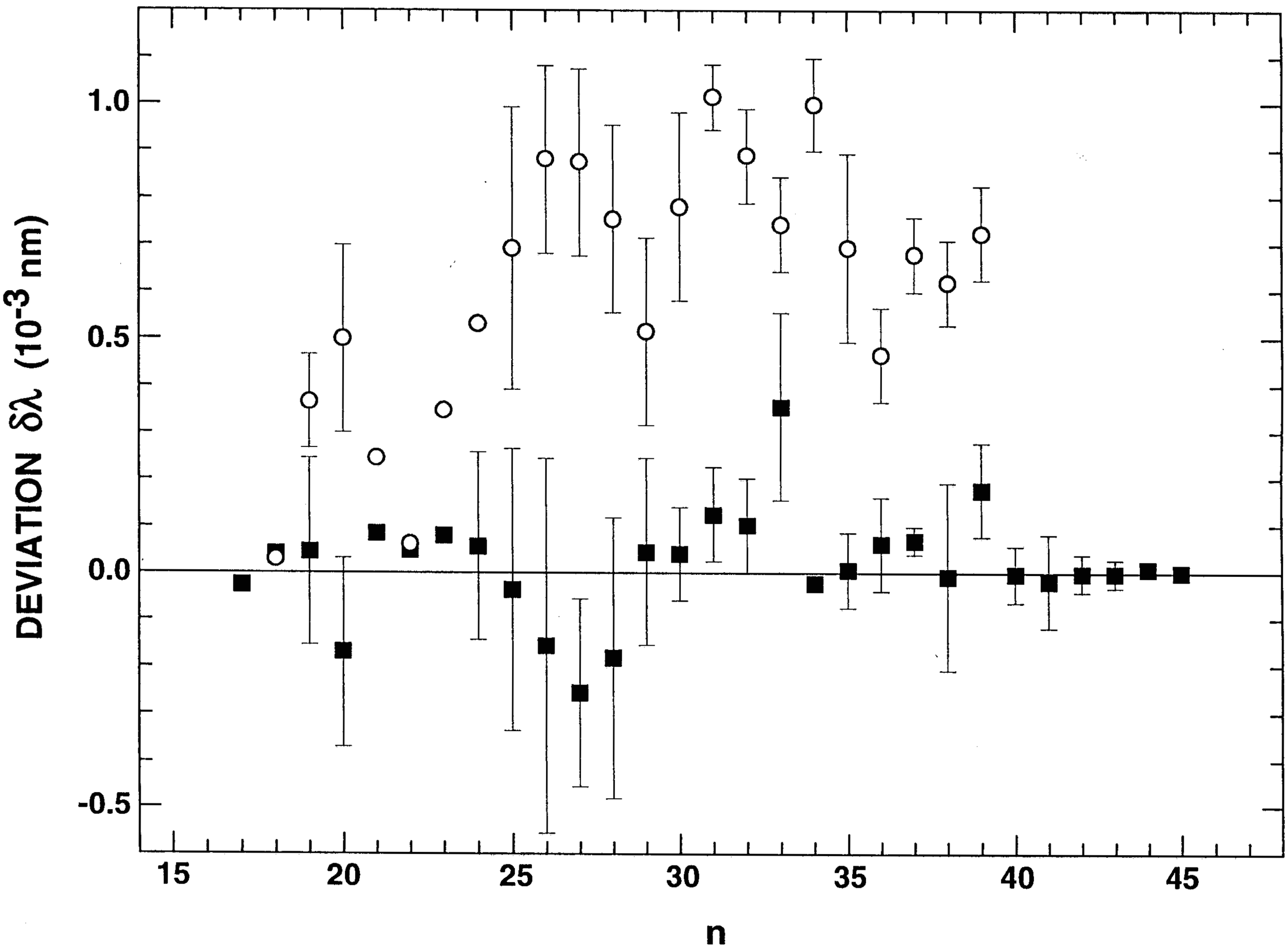

7

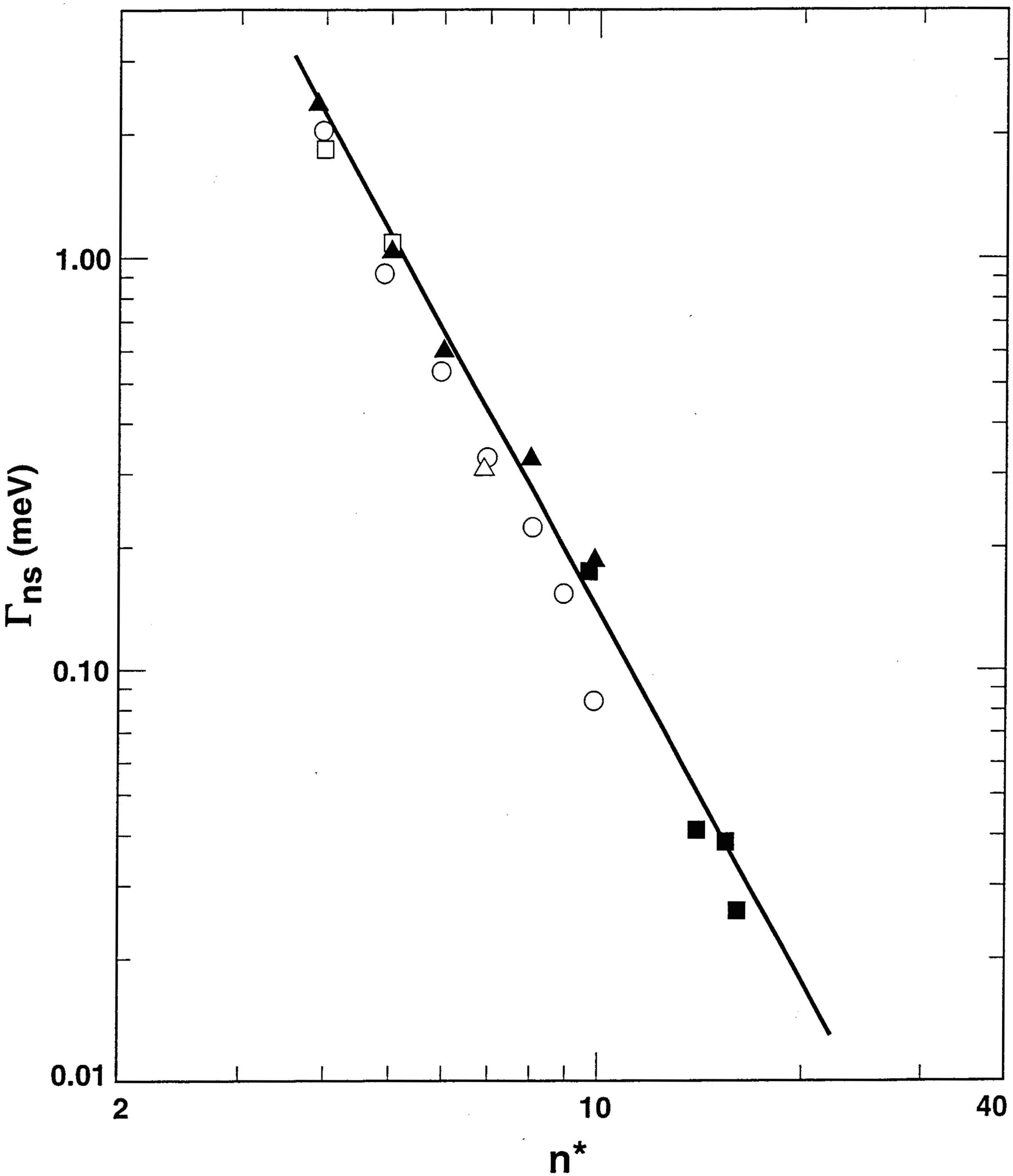
1.00
0.10
0.01
2
10
40
Γ_{ns} (meV)
n*

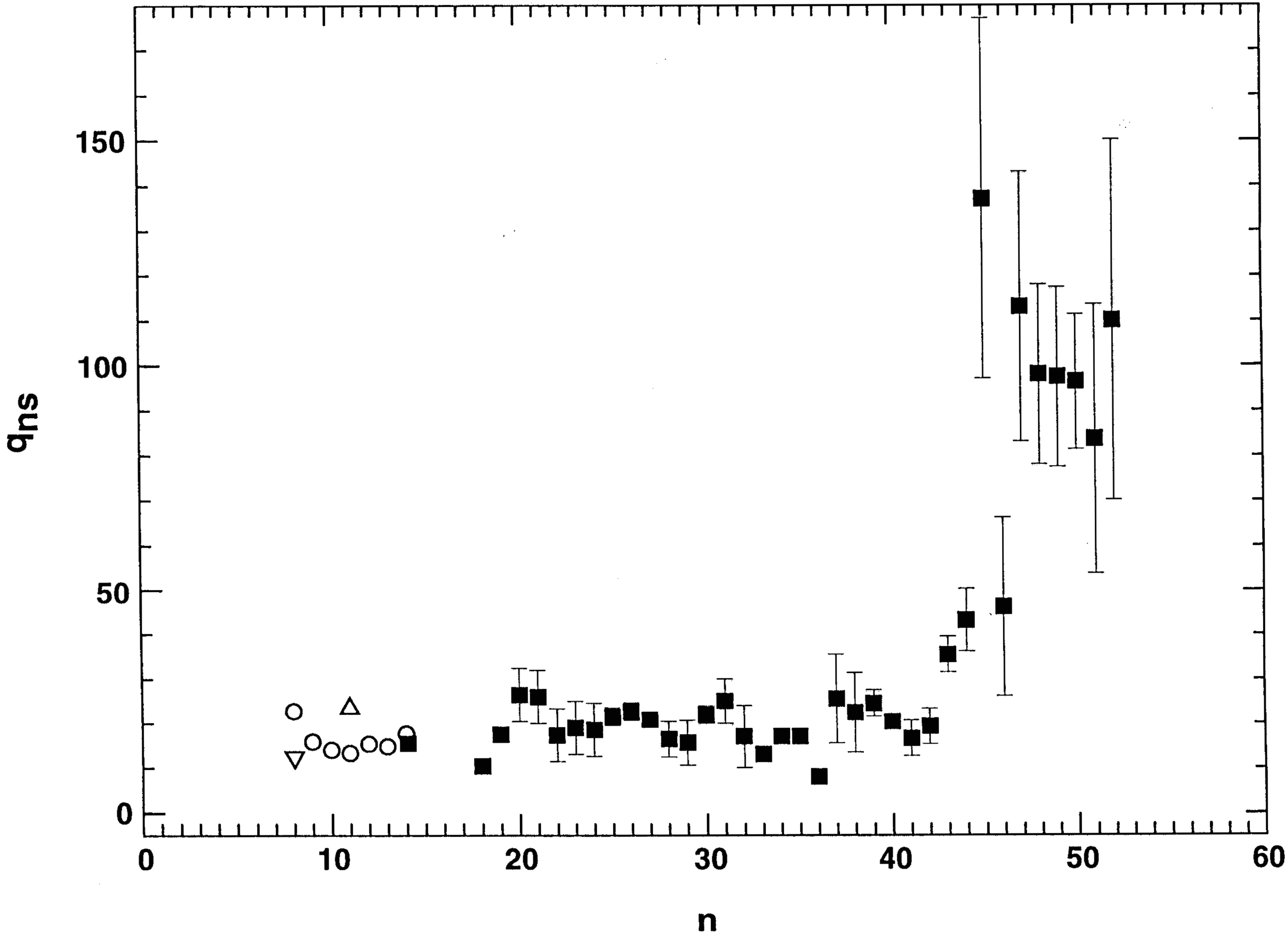

150
100
50
0
q_{ns}
0
10
20
30
40
50
60
n

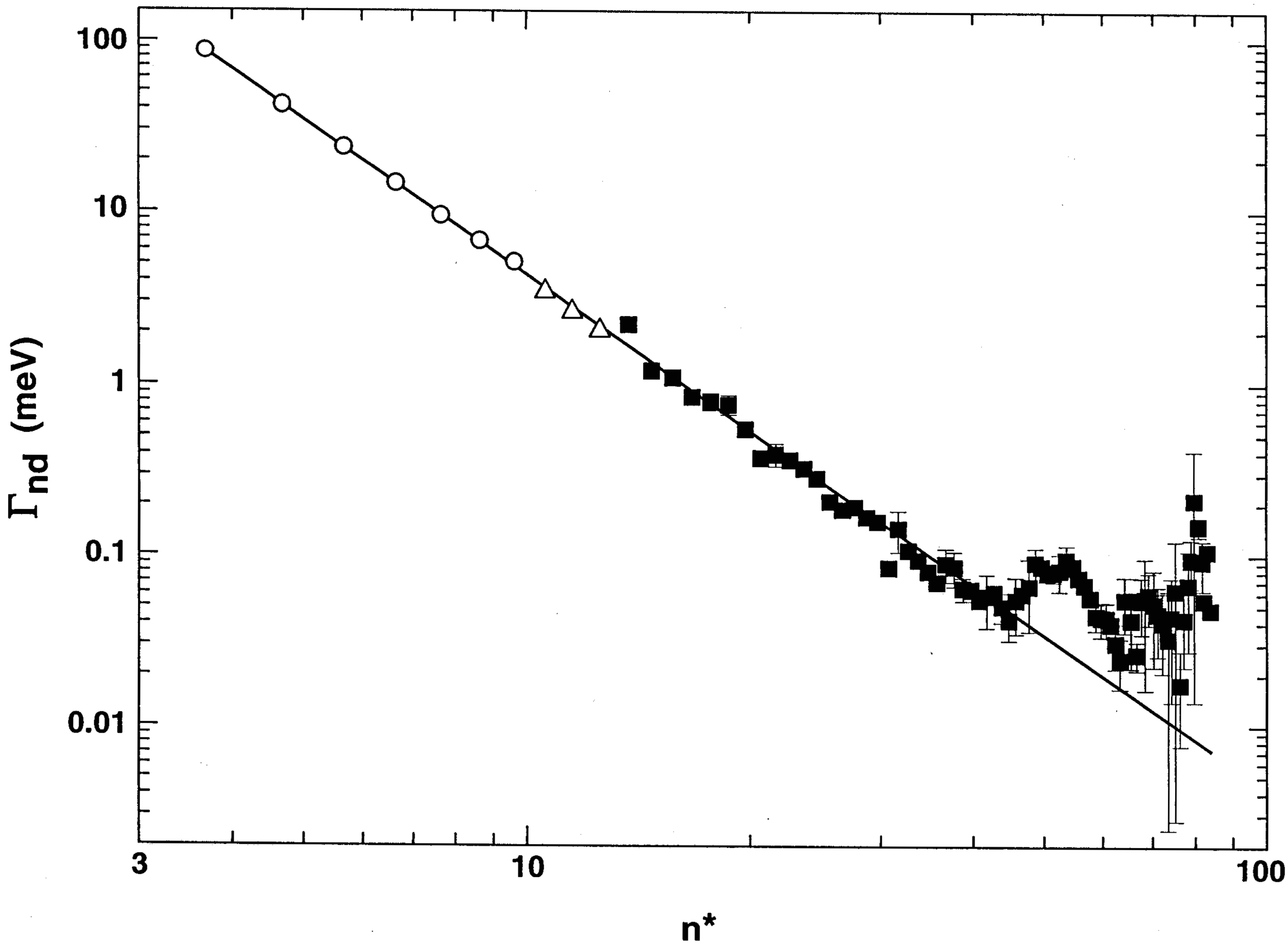

100
10
1
0.1
0.01
Γnd (meV)
3
10
100
n*

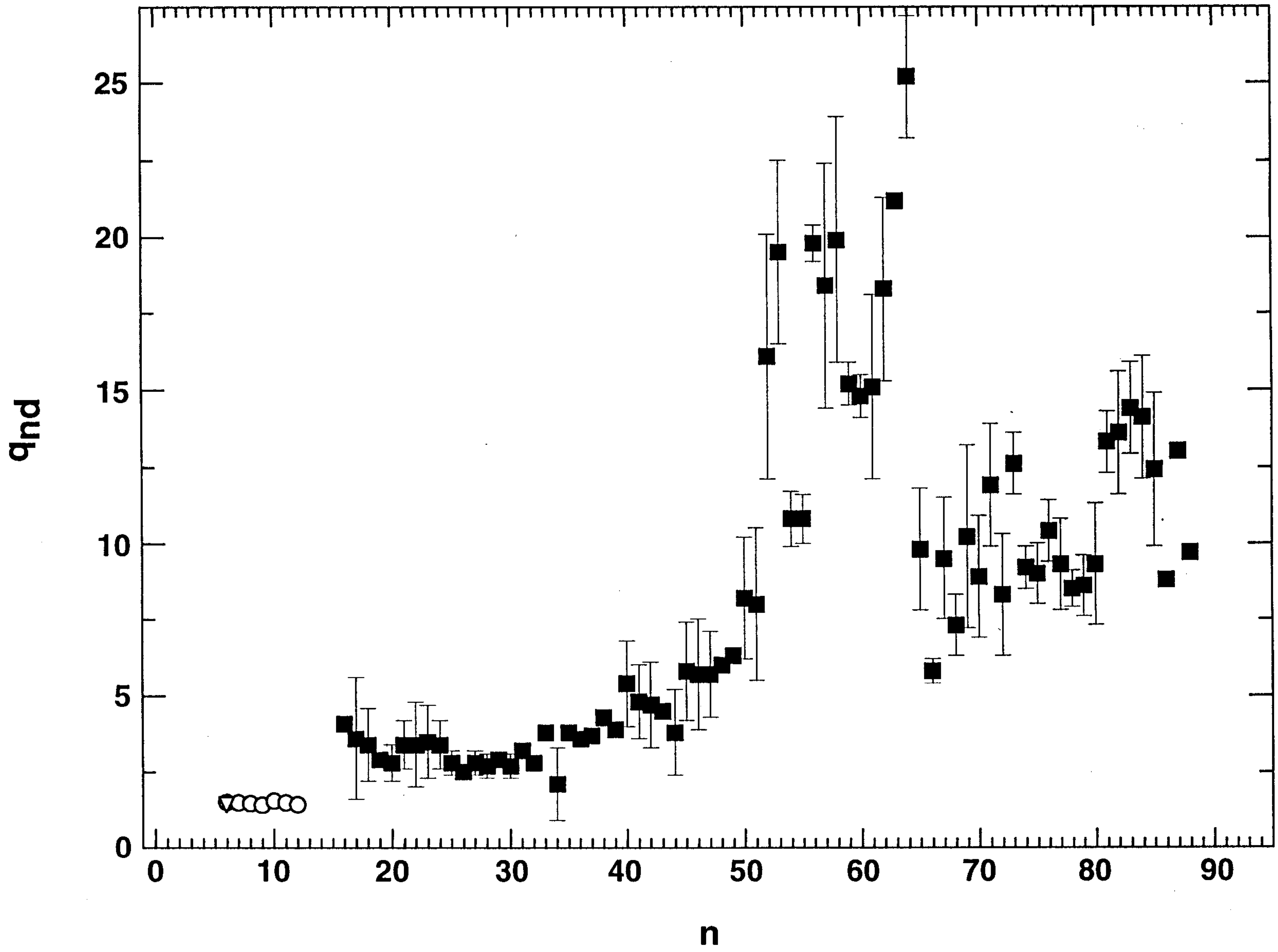

q_{nd}
n
0
5
10
15
20
25
0
10
20
30
40
50
60
70
80
90